ChemistrySelect

Research Article
doi.org/10.1002/slct.202503229

Chemistry Europe
European Chemical Societies Publishing

www.chemistryselect.org

# Comprehensive Molecular Modeling Analysis of Betulin, a Triterpene Isolated from *Miconia burchellii* (Melastomataceae) Native to the Brazilian Cerrado

Marianna C. Silva,*[a] Anderson J.L. Catão,[b] Leonardo L. Borges,[b, c] Antônio S.N Aguiar,[a] Gracielle O.S. Cunha,[d] Dayane C.A. Lima,[d] Antônio C.S. Menezes,[d] Alejandro P. Ayala,[e] and Hamilton B. Napolitano*[b, a]

Betulin, a naturally occurring pentacyclic triterpenoid extracted from Brazilian Cerrado vegetation, was isolated and characterized using single-crystal X-ray diffraction. The solid-state structural analysis revealed H···H contacts and O···H interactions that stabilize the supramolecular architecture, which includes two independent conforms. Additionally, density functional theory calculations at the M06-2X/6-311++G(d,p) level were carried out, providing optimized geometry, electronic distribution insights, and frontier molecular orbitals. The computed HOMO-LUMO energy gap (9.38 eV) suggested moderate chemical reactivity and molecular stability. Furthermore, molecular electrostatic potential mapping highlighted electron-rich regions pertinent to biological interaction. Molecular docking simulations were performed to predict the binding affinity of betulin molecule with cytochrome P450 17A1 – a prostate cancer-associated protein target. The docking outcomes revealed stable interactions and binding sites consistent with reported pharmacological activities. This comprehensive study, combining solid state analysis, advanced molecular modeling, and pharmacophoric analysis, deepens the understanding of structural behavior of betulin and its potential as a bioactive compound.

## 1. Introduction

The Brazilian Cerrado, spanning over 200 million hectares in the country's central region,[1] is the most biodiverse savanna in the world.[2–4] Characterized by a heterogeneous landscape shaped by prolonged dry periods, unique topography, altitude, and soil properties, the Cerrado exhibits various phytophysiognomies.[5,6] The flora within this biome is exceptionally rich in endemic species, contributing to its recognition as a global biodiversity hotspot.[7,8] These unique ecological conditions have driven the evolution of numerous plant species capable of synthesizing secondary metabolites with significant therapeutic potential.[9,10] However, the extensive loss of native vegetation due to urbanization and agribusiness has led to a considerable gap in understanding the biological and medicinal properties of Cerrado plant species.[11] Agricultural expansion, mainly through large-scale soybean and sugarcane monocultures, poses a severe threat to the Cerrado, with projections indicating that 31% to 34% of its remaining areas could be lost by 2050.[12]

*Miconia burchellii*, a species within the diverse yet underexplored genus *Miconia* (Melastomataceae), holds particular significance in the face of environmental pressures. Despite the genus comprising approximately 1,900 species across tropical America, including 282 species in Brazil, only about 2% have been investigated for their phytochemical and pharmacological properties.[13] Research on *Miconia burchellii* could reveal valuable bioactive compounds, enhancing our understanding of its ecological and therapeutic potential. This phytochemical exploration is part of a broader effort to conserve and understand the Cerrado as an essential reservoir of bioactive compounds that produce secondary metabolites with diverse biological activities. Among these compounds, betulin, lup-20(29)-ene-3$\beta$,28-diol (BET)[14,15] has demonstrated significant potential in multiple therapeutic areas, exhibiting anticancer,[16–19] antiviral,[20–23] antimalarial,[20,23] antibacterial,[20,23–26] anti-inflammatory[20,23,27–29] and hepatoprotective[30,23] properties. The anticancer activity of BET is particularly notable, as it has been shown to induce

[a] M. C. Silva, A. S. Aguiar, H. B. Napolitano
Laboratório de Novos Materiais, Universidade Evangélica de Goiás, Anápolis, Goiás, Brazil
E-mail: silva.c.marianna@gmail.com

[b] A. J. Catão, L. L. Borges, H. B. Napolitano
Grupo de Química Teórica e Estrutural de Anápolis, Universidade Estadual de Goiás, Anápolis, Goiás, Brazil
E-mail: hbnapolitano@gmail.com

[c] L. L. Borges
Escola de Ciências Médicas e da Vida, Pontifícia Universidade de Goiás, Goiânia, Goiás, Brazil

[d] G. O. Cunha, D. C. Lima, A. C. Menezes
Laboratório de Produtos Naturais, Universidade Estadual de Goiás, Anápolis, Goiás, Brazil

[e] A. P. Ayala
Departamento de Física, Universidade Federal do Ceará, Fortaleza, Ceará, Brazil

Supporting information for this article is available on the WWW under https://doi.org/10.1002/slct.202503229

© 2025 The Author(s). ChemistrySelect published by Wiley-VCH GmbH. This is an open access article under the terms of the Creative Commons Attribution License, which permits use, distribution and reproduction in any medium, provided the original work is properly cited.



© 2025 The Author(s). ChemistrySelect published by Wiley-VCH GmbH

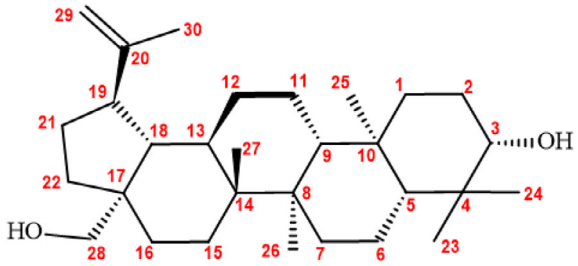



**Figure 1.** Structural formula of the BET with numbering scheme.

apoptosis in cancer cells.[31] Its antiviral properties include efficacy against HIV and other viruses, while its antimalarial activity has demonstrated promise in combating malaria parasites.[23] Given its broad pharmacological potential, BET represents a valuable candidate for pharmaceutical development, emphasizing the urgency of conservation efforts.

BET molecule belongs to the lupane series and comprises a pentacyclic triterpene system with a sterane nucleus. The cyclohexane rings assume a chair conformation, while the cyclopentane ring adopts an envelope conformation. It contains a secondary hydroxyl group at C3, a primary hydroxyl group at C28, and an isopropenyl group at C19 (Figure 1). These structural features make BET a versatile molecule for chemical modifications, enabling the synthesis of numerous derivatives with diverse biological activities.[23,32] The presence of low-polarity lipophilic alkyl fragments in the molecule confers low solubility, making it more affine to low-polarity solvents.[33] Furthermore, thermodynamically unstable intermolecular interactions lead to structural rearrangements and migrations of methyl or hydroxyl groups, which in turn influence its physicochemical properties, including solubility.[34] BET exhibits high lipophilicity, with a log P partition coefficient of 6.17, which enhances its ability to cross biological membranes, facilitating absorption via passive diffusion and distribution in lipid-rich compartments, such as adipose tissue and the central nervous system.[35,36] However, this characteristic also presents disadvantages, such as low water solubility, which can compromise its oral bioavailability and hinder the formulation of efficient drug delivery systems. In general, highly lipophilic compounds tend to undergo accelerated hepatic metabolism, leading to rapid biotransformation and elimination, which can reduce their plasma half-life and, consequently, their therapeutic efficacy.[37]

This study presents a comprehensive report on the isolation and structural characterization of the BET compound. Intermolecular interaction patterns within its supramolecular arrangement were analyzed using Hirshfeld surface (HS) analysis and 2D fingerprint plots. The electronic structure was further explored through density functional theory (DFT), topological descriptors, and Fukui functions to predict chemical reactivity. The integration of experimental data with molecular docking provided deeper insights into BET's binding affinity for its biological target, particularly Cytochrome P450 17A1, thereby reinforcing its therapeutic potential. Finally, pharmacophore analysis supported these findings, enabling the prediction and optimization of molecular properties and biological activities.

## 2. Experimental and Computational Procedures

### 2.1. Plant Material

The stem bark of *Miconia burchellii* Triana (Melastomataceae) was collected in June 2018 in Serra dos Pirineus, Goiás State, Brazil, at three different geographical coordinates: 15°47′3″ S, 48°48′37″ W; 15°47′57″ S, 48°49′10″ W; and 15°47′52″ S, 48°49′53″ W. The species was identified, and voucher specimens (HUEG 13931, 13932, and 13933) were deposited in the Herbarium of the State University of Goiás. Access to the genetic heritage was registered in SisGen under code A4E65A0.

### 2.2. Extraction and Isolation

The botanical material was dried in an air circulation oven at 45 °C for 72 h and then pulverized in a knife mill. The resulting powder (2735 g) was subjected to maceration with ethanol (99.5%, 3 x 4 L) at room temperature. The extracting liquid was then filtered and concentrated on a rotary evaporator, yielding the crude ethanolic extract (103.9 g). This extract was fractionated by vacuum filtration with the incorporation of microcrystalline cellulose D, followed by sequential solvent extraction using hexane, ethyl acetate, and methanol, resulting in the respective fractions: hexane (3.6 g), ethyl acetate (9.0 g), and methanol (25.3 g). A portion of the ethyl acetate fraction (7.0 g of 9.0 g) was further fractionated using a silica gel column (70-230 mesh, 4.5 x 13.0 cm) and eluted with hexane/EtOAc mixtures (8:2, 7:3, 6:4, 5:5, 3:7, v/v), followed by pure EtOAc, yielding subfractions A1-A8. Subfraction A4 (49.0 mg) was subjected to another silica gel column (230-400 mesh, 2.5 x 12.0 cm) and eluted with hexane/EtOAc (8.5:1.5, 7.5:2.5, v/v), affording 29 subfractions, which were pooled into six subfractions (A4.1-A4.6) after thin layer chromatography analysis. Finally, fraction A4.5 (18.0 mg) was identified as BET.

### 2.3. Structural Characterization

Nuclear magnetic resonance (NMR) analyses were performed using a Bruker Avance III spectrometer operating at 11.75 Tesla (500 MHz). $^{1}H$ and $^{13}C$ chemical shifts were acquired using $CDCl_3$ as a deuterated solvent and tetramethylsilane (TMS) as the internal standard. Chemical shifts ($\delta$) are reported in parts per million (ppm). The IR spectra were recorded on a PerkinElmer FTIR Frontier spectrometer using the KBr disc method. The detection wavelength range was set between 4000 and 400 $cm^{-1}$, with 32 scans per spectrum.

The intensity data collection for single-crystal X-ray diffraction was performed using a Bruker Apex II CCD diffractometer equipped with a Photon II CPAD detector and a MoK$\alpha$ radiation source ($\lambda$ = 0.71073 Å) at 273.15 K. The Bruker Saint software package[38] was used for unit cell refinement and data correction, while numerical absorption correction was performed with SADABS.[39] The crystallographic structure was determined using intrinsic/direct phasing methods with the


© 2025 The Author(s). ChemistrySelect published by Wiley-VCH GmbH

ShelXT software[40] and refined via least-squares minimization using the ShelXL refinement package,[41] within the OLEX2 interface.[42] Anisotropic atomic displacement parameters were applied to refine all non-hydrogen atoms. A riding model was used for hydrogen atoms, and their positions were constrained based on the bonded atoms. Their isotropic displacement parameters were set to Uiso(H) = 1.5Ueq(C) for methyl groups and 1.2Ueq(C) for all other hydrogen atoms. Crystallographic tables and structure representations, including thermal-motion probability ellipsoids, were generated using OLEX2,[42] while all supramolecular visualizations were created with Mercury software.[43] Additionally, the PLATON software[44] was used to verify intermolecular interactions, including hydrogen bonds. The crystallographic information file was deposited at the Cambridge Crystallographic Data Center (CCDC)[45] under deposit number 2492953.

### 2.4. Hirshfeld Surface Analysis

The intermolecular interactions were analyzed using HS $d_{\text{norm}}$ mapping, where $d_i$ and $d_e$ represent the internal and external distances, respectively. These parameters indicate donor ($d_i$) and acceptor ($d_e$) regions of intermolecular contacts. The HS $d_{norm}$ map employs a color gradient to represent interaction intensities, with red indicating stronger interactions (shorter distances) and blue representing weaker contacts (longer distances). The $d_{\text{norm}}$ values, ranging from −0.511 to 1.470 Å, provide a detailed view of the spatial distribution of these donor and acceptor regions, improving the understanding of molecular packing. HS was calculated without optimization of geometric parameters, allowing for the visualization and interpretation of potential intermolecular interactions. HS can be understood as crystal partition spaces in which the equation represents electron distribution from the sum of spherical atoms.

$$W(\mathrm{r}) = \frac{\sum_{a\varepsilon molecule}\rho_a(\mathrm{r})}{\sum_{a\varepsilon crystal}\rho_a(\mathrm{r})} \quad (1)$$

In this equation, $W(\mathbf{r})$ is a continuous function with $W(\mathbf{r}) \geq 0.5$. The numerator represents the pro-molecule, while the denominator represents the pro-crystal. The electron density of the atomic fragment is defined as

$$\rho_a(\mathrm{r}) = W_a(\mathrm{r})\,\rho^{mol}(\mathrm{r}) \quad (2)$$

where $\rho^{mol}(r)$ indicates molecular electron density. Normalized contact distances, $d_{\text{norm}}$, are a key aspect of HS analysis. These distances were calculated to highlight the interactions between atoms inside and outside the surface. The parameter $d_i$ represents the distance from an internal atom's nucleus to the HS, indicating a donor region of intermolecular contacts, while $d_e$ represents the distance from an external atom's nucleus to the HS, indicating an acceptor region. The normalized contact distance $d_{\text{norm}}$ is calculated using the equation.

$$d_{norm} = \frac{d_i - r_i^{vdw}}{r_i^{vdw}} + \frac{d_e - r_e^{vdw}}{r_e^{vdw}} \quad (3)$$

where $d_i$ and $d_e$ denote the donor and acceptor regions of intermolecular contacts, respectively, and $r^{vdw}$ represents the Van der Waals radii. On the HS, red indicates shorter distances (stronger interactions), while blue suggests longer distances (weaker interactions).

The 2D fingerprint plot maps all unique intermolecular contacts within a molecule, providing insights into polymorphism and crystal packing by illustrating the electron density distribution around atomic spheres. This plot quantifies the contribution of each interaction to crystalline packing, using a standard range of 0.6-2.8 Å for $d_e$ vs. $d_i$. Overall, HS analysis enhances understanding of molecular packing and polymorphism by offering a detailed view of intermolecular interactions within the crystal.

### 2.5. Theoretical Calculations

All calculations on the BET molecule were performed using DFT, implemented in the Gaussian 16 program package.[46] The molecular geometry was fully optimized in the gas phase without symmetry constraints, starting from crystallographic coordinates. The highly parameterized empirical exchange-correlation functional M06-2X,[46] combined with the diffuse and polarized basis set 6-311++G(d,p)[46] were employed. Additionally, two other density functionals, B3LYP and B97D3, were applied for comparison. Vibrational frequency calculations were performed to confirm that the systems correspond to the global minimum on the potential energy surface. Solvent effects were included by means of the polarizable continuum solvation model IEF-PCM.[46] Electronic structure was analyzed from the FMO, the highest occupied molecular orbital (HOMO) and the lowest unoccupied molecular orbital (LUMO). Nucleophilic and electrophilic regions were predicted by the molecular electrostatic potential (MEP) maps, in which the electrostatic potential $V(\mathbf{r})$, at the $\mathbf{r}$ point, is defined by the equation.

$$V(\mathrm{r}) = \sum_{\alpha}\frac{Z_\alpha}{|\mathrm{r}_\alpha - \mathrm{r}|} - \int\frac{\rho(\mathrm{r}')}{|\mathrm{r}' - \mathrm{r}|}d\mathrm{r}' \quad (4)$$

where $Z_\alpha$ is the charge of nuclei $\alpha$ at point $\mathbf{r}_\alpha$ and $\rho(\mathbf{r}')$ is the charge density at the point $\mathbf{r}'$. Chemical reactive sites were predicted by the Fukui function, dual descriptor and topological analysis obtained using the Multiwfn package.[47] To gain deeper insight into the intramolecular interactions governing the stability of the BET molecule, a topological analysis based on the Quantum Theory of Atoms in Molecules (QTAIM) was performed using theoretical calculations at the $\omega$B97XD/6-311++G(d,p) level.[48]

### 2.6. Molecular Docking and Pharmacophore Modeling

The BET molecule was analyzed on the web servers for biological activity prediction, molecular targets, and pharmacokinetic properties. The servers used were Pass online[49] (https://www.way2drug.com/passonline/), SwissTargetPrediction[50] (http://www.swisstargetprediction.ch/), and SwissADME[50]


© 2025 The Author(s). ChemistrySelect published by Wiley-VCH GmbH

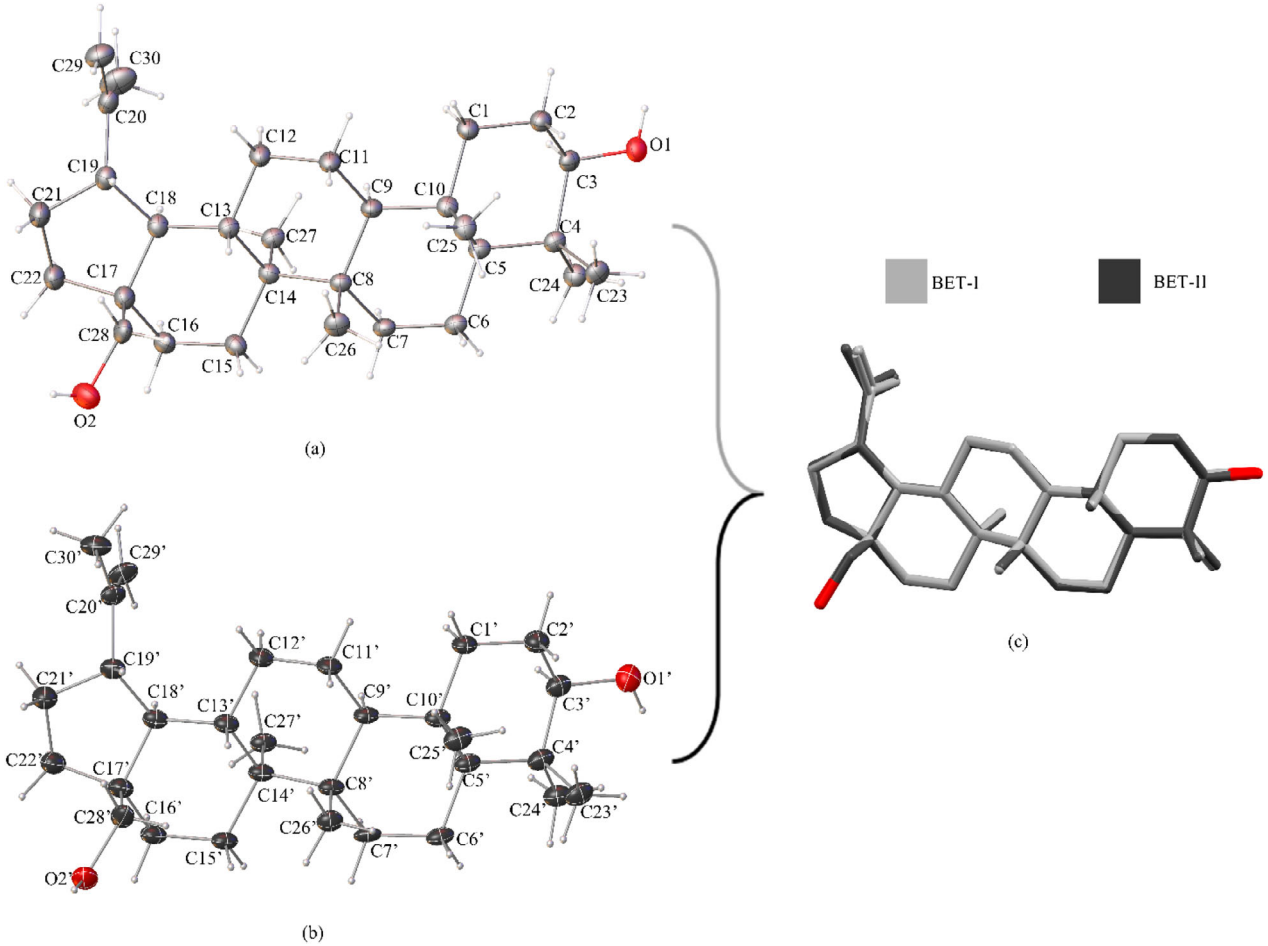



**Figure 2.** ORTEP diagrams of ellipsoids at 30% probability with the atomic numbering scheme for (a) BET-I and (b) BET-II. (c) Structural overlay of BET-I (gray) and BET-II (black), highlighting conformational differences resulting from dihedral angle variations, which indicate the rotation of the methylene group ($CH_2$). Hydrogen atoms were omitted for clarity.

(http://www.swissadme.ch/). Following the evidence of a potential interaction between BET and CYP17A1, the target PDB ID 3RUK (Protein Data Bank, https://www.rcsb.org/) was selected for docking analysis to construct interaction models. Many conformations of BET were simulated (10 best poses were finally selected) in complex with the specified structure of the biological target and the BET to verify that it fit favorably into the ligand binding site of the biomolecule. The target protein was downloaded, and the water molecules were removed. After identifying the active site, the dimensions adopted for the docking were a grid box of 10 Å. The genetic algorithm was employed. GOLD Suite 5.7.0 (Mark Thompson and Planaria Software LLC) generated the docking models. The 2D interaction maps were generated using Discovery Studio 3.5 Visualizer software (https://discover.3ds.com/discovery-studio-visualizer-download), and the 3D images were created with PyMOL Molecular Graphics System, Version 3.1.3 (https://www.pymol.org/). Redocking was performed using a structure in which the target protein and its ligand were co-crystallized to validate the models produced with our selected molecules. Default values were employed for all other parameters, and structures were submitted to 10 genetic algorithm runs using the CHEMPLP fitness function.

To create shared features and pharmacophore models for selective ligands of the Cytochrome P450 17A1, we employed LigandScout v4.5 (https://docs.inteligand.com/ligandscout/).[51] LigandScout identified combinations of shared pharmacophoric features, including hydrogen-bond donors (HBDs), hydrogen-bond acceptors (HBAs), positively and negatively charged groups, hydrophobic (HyPho) regions, and aromatic rings (ARs).[46] These unique pharmacophores were subsequently integrated into the alignment process to develop the Shared Feature Pharmacophore (SFP) model. A literature review was conducted using the databases in Binding DB (https://www.bindingdb.org/rwd/bind/index.jsp) to identify compounds with Cytochrome P450 17A1 antagonist activity. Five compounds with the lowest inhibitory concentration ($IC_{50}$) values were included in a dataset used to obtain pharmacophore models.

## 3. Results and Discussion

### 3.1. Solid-State Characterization

The $^1$H NMR spectrum of BET (Figure S1) exhibited a doublet at $\delta_H$ 4.70 (1H, *d*, $^2J$ = 1.8 Hz) and a multiplet at $\delta_H$ 4.60 (1H, *m*),


© 2025 The Author(s). ChemistrySelect published by Wiley-VCH GmbH

corresponding to the olefinic hydrogen H-29, characteristic of triterpenes with a lupane skeleton. The signals observed at $\delta_H$ 3.81 (1H, *dd*, $^2J$ = 10.8 and 1.2 Hz) and $\delta_H$ 3.35 (1H, *d*, $^2J$ = 10.8 Hz) were assigned to the diastereotopic methylene hydrogen atoms bonded to the hydroxyl (H-28). The signal centered at $\delta_H$ 3.20 (1H, *dd*, $^3J$ = 11.4 and 4.9 Hz) was attributed to the H-3 hydrogen bonded to the carbinolic carbon. The coupling constant ($J$ = 11.4 Hz) indicated that H-3 is in the axial position and couples with H-2 $\beta$ in a diaxial arrangement. The signal centered at $\delta_H$ 2.40 (1H, *m*) was assigned to H-19. Additionally, five singlets corresponding to methyl hydrogens were also observed at $\delta_H$ 1.04 (3H, *s*), $\delta_H$ 1.00 (3H, *s*), $\delta_H$ 0.99 (3H, *s*), $\delta_H$ 0.85 (3H, *s*), and $\delta_H$ 0.78 (3H, *s*), which were attributed to H-26, H-23, H-27, H-25, and H-24, respectively. An additional singlet was observed at $\delta_H$ 1.70 (3H, *s*), characteristic of methyl hydrogens attached to an unsaturated carbon. The $^{13}$C NMR spectrum (Figure S2) displayed signals at $\delta_C$ 150.5 and $\delta_C$ 109.7, corresponding to the olefinic carbons C-20 and C-29, respectively. The signals at $\delta_C$ 79.0 and $\delta_C$ 60.6 were assigned to the carbinolic carbons C-3 and C-28, respectively.

In the IR spectrum of BET (Figure S3), a broad absorption band at 3432 cm$^{-1}$ corresponds to the vibrations of hydroxyl groups. The stretching modes of the =CH$_2$ group are observed at 3075 cm$^{-1}$, while those of the C–H groups are observed as a series of bands at 2942 and 2867 cm$^{-1}$. The vibrations of the C=C bond are detected at 1687 and 1643 cm$^{-1}$. The CH$_2$ group vibrations are assigned to 1452 cm$^{-1}$, whereas the CH$_3$ group is attributed to the band at 1375 cm$^{-1}$. The stretching mode of the C–O group is observed as a band at 1033 cm$^{-1}$. The ORTEP diagram (Figure 2a,b) shows two independent conforms of BET, which crystallize in the monoclinic noncentrosymmetric space group P2$_1$, with (BET-I and BET-II). The overlap of BET-I and BET-II (RMSD = 0.0641°) reveals the geometric differences between the two structures arise from variations in their dihedral angles: C18–C19–C20–C29 (–138.51 (2)°) and C18–C19–C20–C30 (43.17 (3)°) in BET-I, C18′–C19′–C20′–C29′ (32.76 (3)°) and C18′–C19′–C20′–C30′ (−154.51 (2)°) in BET-II (Figure 2c). The crystallographic parameters and structural refinement are presented in Table 1.

The crystal packing exhibits a well-defined layered organization, characterized by a 2-fold screw axis parallel to the *b*-axis, as illustrated in Figure 3a. This packing is stabilized by a combination of key intermolecular interactions, which significantly contribute to the structural cohesion and organization of the molecules within the crystal lattice, as demonstrated in Table 2. Specifically, the O2–H2···O2′ and O1′–H1′···O2 hydrogen bond follows a linear pattern along the *a*- and *b*-axes and can be described by the $C_2^2(16)$ graph set.[52] Additionally, the C22–H22B···O1 interaction further enhances the crystal's structural integrity. This interaction forms a chain-like arrangement along the *b*-axis and is described by the $C_1^1(13)$ motif[52] (Figure 3b).

Intermolecular interactions were analyzed using the HS, as shown in Figure 4. The molecule inside the surface corresponds to BET-I; the red dots (1) and (3) correspond to $d_i$ contacts, indicating that the molecule acts as a donor in the O2–H2···O2′ and C22–H22B···O1 interactions, respectively. In contrast, the red dot (2) corresponds to $d_e$ contacts, indicating where the molecule functions as an acceptor in O1′–H1′···O2. Other regions on the surface exhibit H···H interactions, which, due to their weak van der Waals nature, are not highlighted as dominant contributors.

**Table 1.** Crystallographic data and structure refinement for BET.

| | | |
|---|---|---|
| Chemical formula | $C_{30}$ $H_{50}O_2$ | |
| Formula weight | 442.70 | |
| Crystal system, space group | Monoclinic, P2$_1$ | |
| Temperature (K) | 273 | |
| Unit cell dimensions | $a$ = 7.142(2) Å<br>$b$ = 29.894(9) Å<br>$c$ = 12.609(4) Å | $\alpha$ = 90 (5)°<br>$\beta$ = 91.249(10)°<br>$\gamma$ = 90 (5) ° |
| Volume | 2691.5(13) | |
| Radiation type | Mo $K\alpha$ | |
| Absorption coefficient (mm$^{-1}$) | 0.066 | |
| F (000) | 984 | |
| Final $R$ índices [$F^2 > 2\sigma$ ($F^2$)] | $R_1$ = 0.1050, w$R_2$ = 0.2535 | |
| $R$ indices (all data) | $R_1$ = 0.2055 w$R_2$ = 0.3316 | |
| Goodness-of-fit on F$^2$ | 1.012 | |
| No. of reflections | 5615 | |
| No. of parameters | 594 | |
| $\Delta\rangle_{max}$, $\Delta\rangle_{min}$ (e Å$^{-3}$) | 0.39, −0.28 | |

Figure 5 presents the fingerprint plot interactions, highlighting that weak H···H contacts ($d_e = d_i$ = 1.2 Å) dominate the intermolecular interactions, comprising 91.9% of the HS. H···O contacts represent the second most significant contribution, accounting for 5.0% of the total surface area. In contrast, the compound shows no significant stabilization through H···C or $\pi\cdots\pi$ interactions, accounting for just 0.2% of the total surface area. The combination of $d_e$ and $d_i$ distance functions effectively maps all intermolecular contacts within the molecule and quantifies their relative contributions. This analysis provides a distinct fingerprint for each compound, offering insight into its crystal packing and interaction profile.

### 3.2. Molecular Modeling Description

The total energies for three different density functionals present close values, as show in Table 3, which also list the HOMO and LUMO's energies. The HOMO-LUMO gap shows that the molecule absorbs wavelengths only in the UV region, as also obtained from TDDFT calculations, with absorption below 177 nm (see the UV–vis spectrum in Figure S4 and Table S1). The calculated IR spectrum is also provided in Figure S5. HOMO and LUMO orbitals (Figure 6) are localized at C20-C30 alkene site, a very reactive site of the molecule, for which many chemical manipulations of BET have been reported, such as oxidation, allylic halogenation, allylic trifluoromethylation and so on. Figure 6 also shows the MEP of the BET molecule, featuring two minima and two maxima around the hydroxyl groups of the molecule.

Topological analysis shows 189 critical points (CPs) which 83 are nuclei CPs, 93 are bond CPs, 13 are ring CPs, and 1 is a cage CP.


© 2025 The Author(s). ChemistrySelect published by Wiley-VCH GmbH

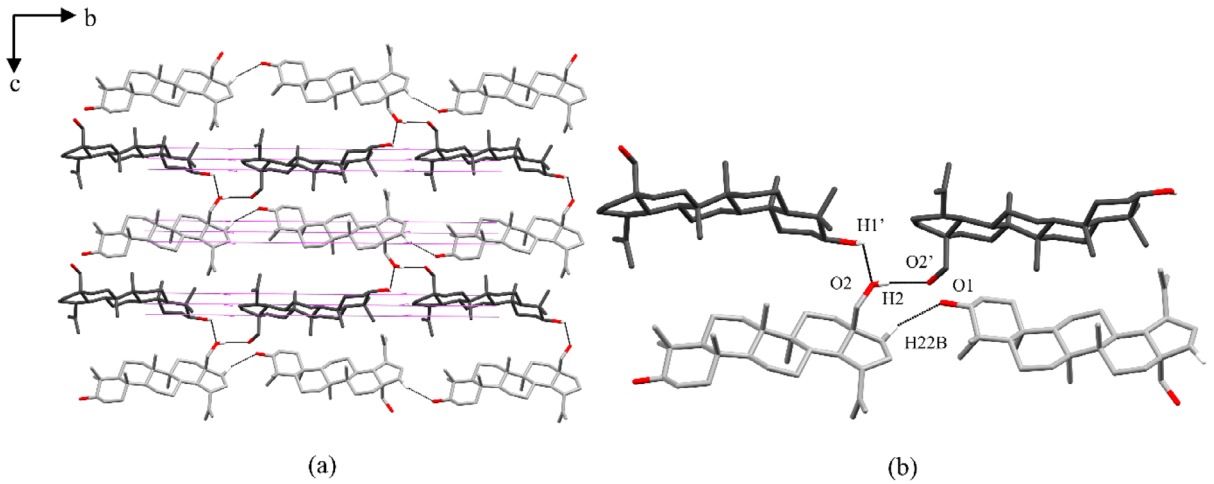



**Figure 3.** (a) Illustration of the crystal packing of BET, where BET-I is represented by gray and BET-II by black, highlighting the 2-fold symmetry element with purple lines. (b) Depiction of the intermolecular interactions responsible for stabilizing the crystal packing. Hydrogen atoms not participating in these interactions have been excluded for clarity.

**Table 2.** Geometric parameters of intermolecular interactions for BET.

| D–H···A | D–H/Å | H···A/Å | D···A/Å | D–H···A/degree | Symmetry code |
|---|---|---|---|---|---|
| O1′–H1′···O2 | 0.82 | 2.37 | 2.79(3) | 112 | $-1+x, y, 1+z$ |
| O2–H2···O2′ | 0.82 | 2.22 | 3.03(3) | 171 | $-2-x, -\frac{1}{2}+y, -1-z$ |
| C22–H22B···O1 | 0.97 | 2.58 | 3.50(3) | 159 | $-1-x, \frac{1}{2}+y, -1-z$ |

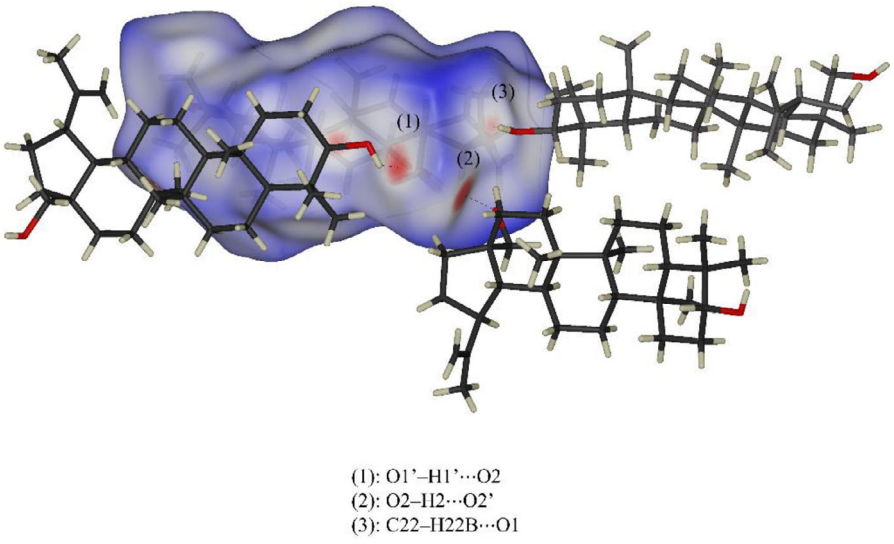



**Figure 4.** Hirshfeld surfaces $d_{norm}$ indicating intermolecular contacts (1) O1′–H1′···O2, (2) O2–H2···O2′ and (3) C22–H22B···O1 for BET, represented by dashed lines.

The optimized structures in the gas and aqueous phases were analyzed and the results were similar. In addition to the common chemical bonds, seven intramolecular interactions formed pathways between the BCPs (see Figure S6a). Among these, the C12—H—C20 interaction (See Figure 1 for numbering) and C12—H—-H—C30 form a region with two ring CPs showing a region of high electronic density, which is essential for understanding the molecule's reactivity as shown by Fukui analysis. The CP cage is above the six-membered ring formed by C5-C6-C7-C8-C9-C10 (see Figure S6b) and can provide the structure with conformational stability. Orbital contributions to density difference were evaluated using the orbital-weighted Fukui function and dual


© 2025 The Author(s). ChemistrySelect published by Wiley-VCH GmbH

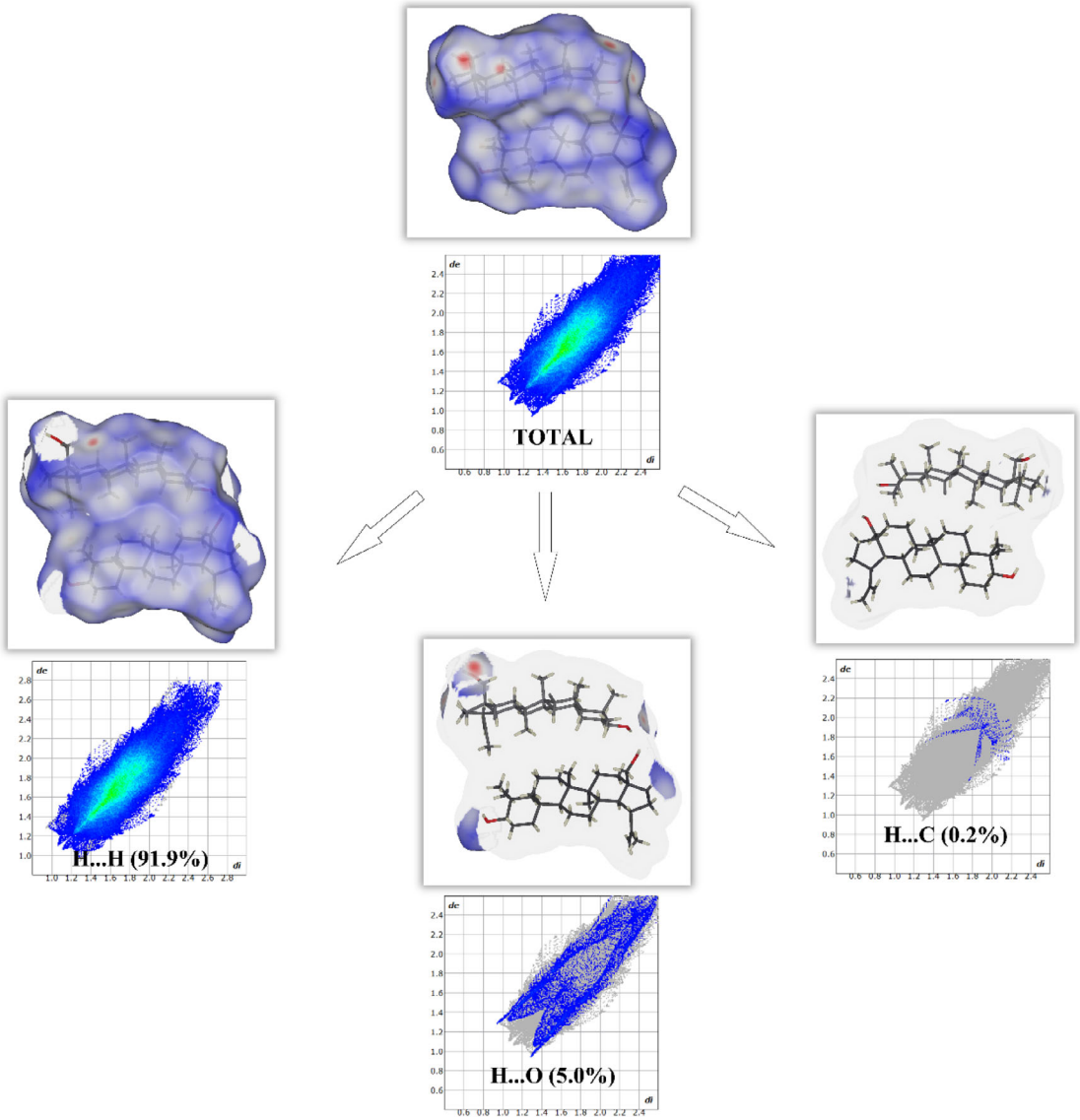



**Figure 5.** Fingerprint analysis and quantification of total interactions in BET.

**Table 3.** Electronic structure parameters of the BET molecule.

| Functional | Total energy (Hartree) | Dipole moment (Debye) | HOMO (eV) | LUMO (eV) | HOMO-LUMO GAP (eV) |
|---|---|---|---|---|---|
| B3LYP | −1324.0612 | 2.87 | −6.74 | 0.29 | 7.03 |
| B97D3 | −1323.2665 | 2.76 | −5.64 | −0.44 | 5.20 |
| M062X | −1323.5119 | 2.95 | −8.01 | 1.37 | 9.38 |
| M062X - Water | −1323.5224 | 3.89 | −7.98 | 1.40 | 9.37 |

descriptor for the BET molecule. The results are presented in Table 4 and the reactive sites are represented in Figure 7.

In Figures 7 and S7, the region above and below the CC double bond plane has a large positive $f^-$ and prominent negative dual descriptor $\Delta f$ which corresponds to the site having remarkable nucleophilicity, i.e., vulnerable to electrophilic attack, such as electrophilic addition reactions. In the region of $\Delta f > 0$, the site is favorable for a nucleophilic attack, which is in accordance with the second step of electrophilic addition, i.e., the nucleophilic attack to the formed cation (see $f^-$) acting as an electrophile and accepting an electron pair from the nucleophile.

### 3.3. Molecular Docking and Pharmacophore Modeling

Regarding the pharmacokinetic aspects, the BET molecule can be classified as drug-like according to Lipinski's criteria. It does not have permeability to the blood-brain barrier and appears not


© 2025 The Author(s). ChemistrySelect published by Wiley-VCH GmbH

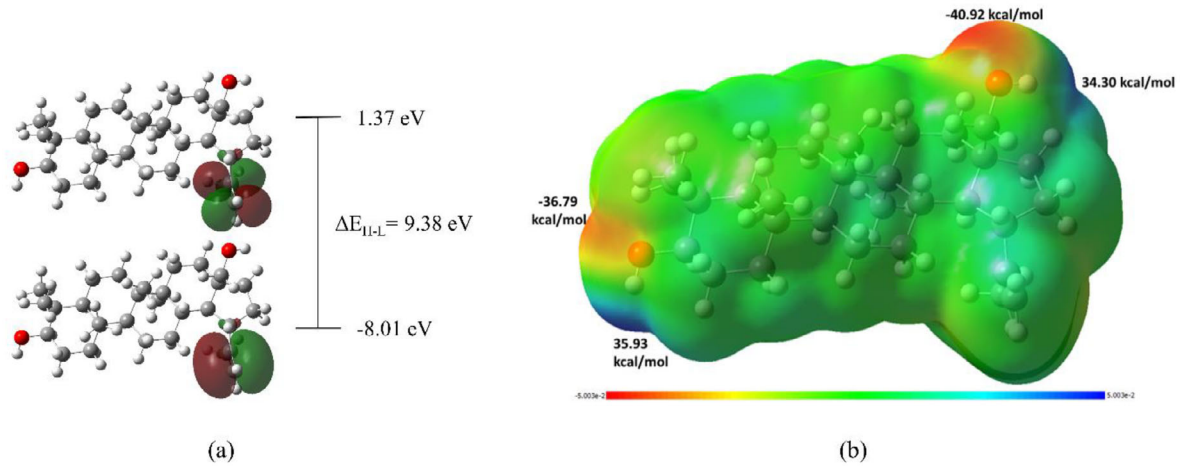



**Figure 6.** Electronic properties of BET molecule. (a) Isosurfaces of the FMO, HOMO and LUMO (isovalue = 0.02 a.u.), illustrating electron density distribution and molecular reactivity. (b) A MEP at $\rho(r) = 4.0 \times 10^{-4}$ electrons/Bohr$^3$ contour of the total SCF electron density, highlighting regions of electrophilic and nucleophilic character, at M06-2X/6-311++G(d,p) level of theory.

**Table 4.** Global indices of the Fukui analysis for the BET molecule.

| Electron density | EE (Hartree) | Homo energy (eV) | VIP (eV) | VEA (eV) | ME (eV) | $\mu$ (eV) | Hardness (eV) | Softness (eV$^{-1}$) | Electro-philicity index | Nucleophi-licity index |
|---|---|---|---|---|---|---|---|---|---|---|
| E(N) | −1323.5119 | −8.68 | 8.64 | −1.98 | 3.33 | −3.33 | 10.62 | 0.094 | 0.52 | 0.44 |
| E(N + 1) | −1323.4392 | 11.71 | | | | | | | | |
| E(N-1) | −1323.1942 | −12.09 | | | | | | | | |

EE stands for electronic energy; VIP stands for Vertical Ionization Potential; VEA stands for Vertical Electron Affinity; ME stands for Mulliken electronegativity; $\mu$ means the Chemical Potential.

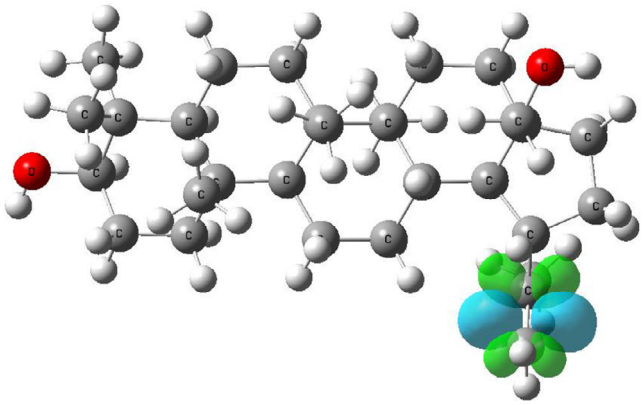


**Figure 7.** Isosurface map of orbital-weighted dual descriptor evaluated in terms of electron density surfaces of the BET molecule at isovalue = $1.0 \times 10^{-3}$ electrons/Bohr. Green and blue isosurfaces correspond to the positive and negative region of the orbital-weighted function.

to inhibit cytochromes related to metabolism, such as CYP450 1A2, CYP450 2C19, CYP450 2C9, CYP450 2D6, and CYP450 3A4. These low interactions with metabolically relevant cytochrome P450s would minimize the potential for interactions with pharmaceutical substances. An antineoplastic effect was observed in the biological predictive analyses conducted using the PASS prediction server, with values of Pa = 0.95 and Pi = 0.004. This information and the molecular target prediction analysis directed the investigation toward CYP450 17A1.

The in silico predictions of BET regarding potential molecular targets indicate a possible interaction with cytochrome P450 17A1. Redocking of the co-crystallized ligand (abiraterone) with the target CYP450 17A1 was successfully performed, and this model was also employed for BET docking.[53] All RMSD values were less than 0.6 A. In its active site, the primary amino acids involved in these interactions are ASP298 (through a reinforced hydrogen bond) and ARG239 (hydrogen bond). Hydrophobic interactions are observed with the residues THR306, GLY301, VAL483, ILE371, and PHE114, all of which are located at the active site of chain A of the protein (Figure 8a,b).

The results of the pharmacophoric modeling appear to corroborate the findings obtained from the molecular docking analysis (Figure 9). Through pharmacophoric modeling with the five most potent CYP450 17A1 inhibitors, four spatial features were observed: a hydrogen bond acceptor group and three hydrophobic groups. These interactions are evident in the 2D interaction map, with the designated target highlighted (Figure 10). There is considerable evidence indicating that the molecule BET has antitumoral effects, including in prostate cancer. One of the targets related to the treatment and prevention of prostate cancer is cytochrome 17A1.[53–55]

There is considerable evidence indicating that the molecule BET has antitumoral effects, including in prostate cancer.[56] One of the targets related to the treatment and prevention of prostate cancer is cytochrome 17A1. In the study by Chrobak and colleagues (2019),[57] BET derivatives (3-phosphate compounds)


© 2025 The Author(s). ChemistrySelect published by Wiley-VCH GmbH

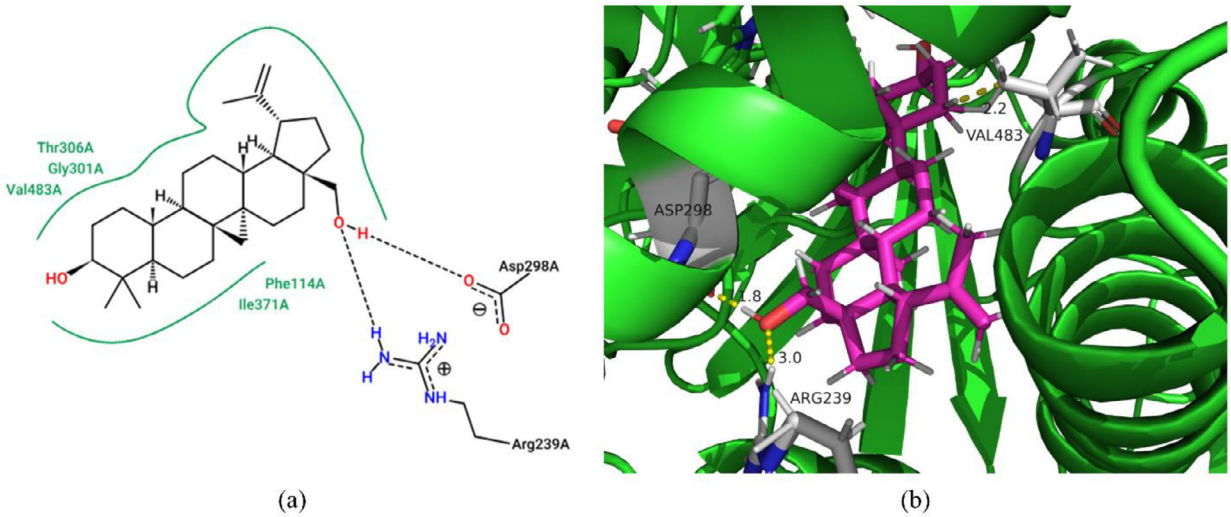



**Figure 8.** Molecular docking analysis of BET in the active site of Cytochrome P450 CYP17A1. This figure provides insights into BET interaction patterns and binding conformations compared to a known inhibitor. (a) 2D interaction diagram of BET bound to Cytochrome P450 CYP17A1 in conformation 1, generated using PoseView interface (https://www.zbh.uni-hamburg.de/en/forschung/amd/server/poseview.html). (b) BET docked in the ligand-binding site of Human Cytochrome P450 CYP17A1 in conformation 1 (PLP Chemscore 1.77), visualized with Pymol 3.1.3. Distance values are given in Å.

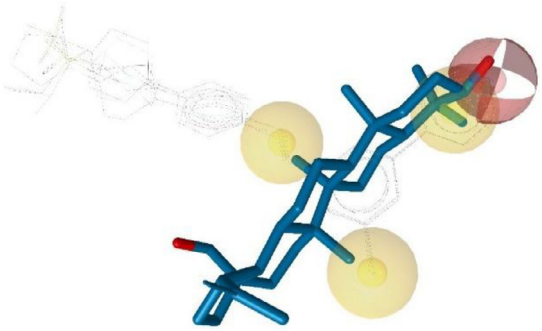


**Figure 9.** 3D model of shared featured pharmacophore between BET and the Cytochrome P450 CYP17A1 ligands. The pharmacophore features are color-coded for hydrogen-bond acceptors (red) and hydrophobic (yellow). The five compounds used in this analysis were BDBM330383, BDBM330386, BDBM330388, BDBM330389, and BDBM330390, which are the codes of the compounds listed on the website (https://www.bindingdb.org/rwd/bind/index.jsp, accessed on February 9, 2025).

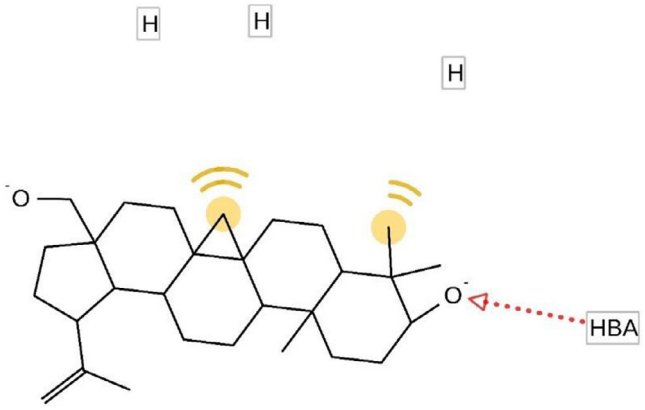



**Figure 10.** Individual pharmacophores of BET shared with five Cytochrome P450 CYP17A1 ligands, with the lowest IC50. Hydrogen-bond acceptor (HBA), hydrophobic (H), and aromatic ring (AR).

synthesized exhibited in vitro effects against a range of tumor cells, such as human leukemia (MV-4-11 and CCRF/CEM), lung carcinoma (A549), prostate cancer (DU 145), melanoma (Hs 294T) cell lines, and murine leukemia P388. In this same study, the following targets were investigated by in silico tools: topoisomerase I and II, epidermal growth factor receptor (EGFR) and vascular endothelial growth factor (VEGFR), transcription factor NF-$\kappa$B, antiapoptotic protein Bcl-2, and peroxisome proliferator-activated receptor (PPAR$\gamma$). In addition to these targets, the predictive analyses suggest another target may be related to prostate cancer, such as CYP450 17A1. This target has been extensively investigated, particularly in evaluating its potential for interaction with other compounds of natural origin.[58]

In addition to CYP17A1, predictive analyses indicated that betulin may also interact with two other relevant molecular targets: CYP19A1 (aromatase) and CYP2C19. CYP19A1 is a key enzyme in estrogen biosynthesis and is an established target for therapies against hormone-dependent breast cancers. CYP2C19 is primarily involved in the hepatic metabolism of drugs, playing a crucial role in the processing of numerous medications. The potential binding of betulin to these enzymes not only broadens its pharmacological profile as a potential antitumor agent but also raises essential flags for possible drug-drug interactions and off-target effects if administered in combination with other therapies.[59,60]

## 4. Conclusions

This work thoroughly characterized BET molecule extracted from the Brazilian Cerrado through an integrated approach. The HS analysis unveiled critical insights into the molecular interactions within the crystal lattice, revealing that H···H contacts were predominant, while O···H interactions significantly contributed to stabilizing the structure. These contacts underscore the role of hydrogen bonding and van der Waals forces in shaping 3D


© 2025 The Author(s). ChemistrySelect published by Wiley-VCH GmbH

organization of BET, influencing its physicochemical properties and potential biological behavior. Although the supramolecular arrangement highlights the stabilizing role of BET in the solid state, its stability under physiological conditions is limited by poor aqueous solubility and rapid metabolism.

Theoretical studies using DFT at the M06-2X/6-311++G(d,p) level offered optimized geometry and electronic structure characterization, including FMO and MEP. These calculations corroborated the experimental structural data and clarified essential electronic features like charge distribution and reactive regions. The HOMO-LUMO gap (9.38 eV) indicated moderate molecular reactivity, consistent with the compound's capacity for biological interaction. Molecular docking simulations were carried out to explore BET's anticancer potential, highlighting stable binding conformations and significant interactions with key amino acid residues. Energy-minimized conformations and frontier molecular orbital distributions provide a structural basis for the observed activity. The results indicate that the hydroxylated and esterified derivatives of betulin exhibit enhanced electron-donating capacity.

Furthermore, in silico predictions suggested potential interaction of BET with cytochrome P450 17A1, a target associated with prostate cancer treatment, pointing to the molecule's candidacy for further in vitro validation. These insights are crucial for understanding how BET might interact in biological systems, supporting its relevance in drug design. Overall, this work contributes to the structural and molecular understanding of natural compounds and emphasizes the importance of integrating crystallographic surface and theoretical analyses to predict and evaluate their pharmacological profiles.

## Acknowledgments

The authors are grateful to the Conselho Nacional de Desenvolvimento Científico e Tecnológico (CNPq) and the Fundação de Amparo à Pesquisa do Estado de Goiás (FAPEG) for financial support. They thank Prof. Dr. Mirley Luciene dos Santos for identifying the species collected. The authors are also grateful to the High-Performance Computing Center of the Universidade Estadual de Goiás (UEG) for theoretical calculations.

The Article Processing Charge for the publication of this research was funded by the Coordenacao de Aperfeicoamento de Pessoal de Nivel Superior - Brasil (CAPES) (ROR identifier: 00x0ma614).

## Conflict of Interests

The authors declare no conflict of interest.

## Data Availability Statement

The data that support the findings of this study are available in the supplementary material of this article.

**Keywords:** Betulin · Brazilian cerrado · DFT · Molecular docking · X-ray diffraction

[1] B. B. N. Strassburg, T. Brooks, R. Feltran-Barbieri, A. Iribarrem, R. Crouzeilles, R. Loyola, A. E. Latawiec, F. J. B. O. Filho, C. A. d. M. Scaramuzza, F. R. Scarano, B. Soares-Filho, A. Balmford, *Nat. Ecol. Evol.* **2017**, *1*, 1–3.
[2] G. R. Colli, C. R. Vieira, J. C. Dianese, *Biodivers. Conserv.* **2020**, *29*, 1465–1475.
[3] J. F. Silva, M. R. Fariñas, J. M. Felfili, C. A. Klink, *J. Biogeogr.* **2006**, *33*, 536–548.
[4] M. C. Silva, L. O. Sallum, A. C. S. Menezes, A. J. Camargo, H. B. Napolitano, *ChemistrySelect* **2019**, *4*, 14012–14020.
[5] E. Bailão, I. Devilla, E. da Conceição, L. Borges, *Int. J. Mol. Sci.* **2015**, *16*, 23760–23783.
[6] M. Silva, V. Duarte, L. Sallum, G. Cunha, J. Custodio, A. Oliver, J. Peixoto, A. Menezes, H. Napolitano, *J. Braz. Chem. Soc.* **2023**, *34*, 1293–1302.
[7] N. Myers, R. A. Mittermeier, C. G. Mittermeier, G. A. B. da Fonseca, J. Kent, *Nature* **2000**, *403*, 853–858.
[8] M. C. Silva, G. Cunha, P. Firmino, L. O. Sallum, A. Menezes, J. Dutra, J. de Araujo-Neto, A. A. Batista, J. Ellena, H. B. Napolitano, *ACS Omega* **2023**, *8*, 40764–40774.
[9] C. M. L. Cardozo, A. C. Inada, G. Marcelino, P. S. Figueiredo, D. G. Arakaki, P. A. Hiane, C. A. L. Cardoso, R. D C. A. Guimarães, K. D. C. Freitas, *Molecules* **2018**, *23*, 2336.
[10] J. D. Rocha, F. M. Carneiro, A. S. Fernandes, J. M. Morais, L. L. Borges, L. Chen-Chen, L. M. de Almeida, E. F. L. C. Bailão, *Int. J. Mol. Sci.* **2022**, *23*, 3413.
[11] K. C. D. Laste, G. Durigan, A. N. Andersen, *Austral. Ecol.* **2019**, *44*, 313–326.
[12] J. D. C. Peixoto, B. J. Neves, F. G. Vasconcelos, H. B. Napolitano, M. G. D. S. Barbalho, S. D. E. Silva, L. P. Rosseto, *Molecules* **2019**, *24*, 2891.
[13] G. O. S. Cunha, D. M. da Silva, M. L. dos Santos, M. O. d. M. Filho, C. do Ó Pessoa, C. de Jesus Guimarães, M. F. S. Silva, A. C. S. Menezes, *S. Afr. J. Bot.* **2021**, *137*, 345–350.
[14] M. N. Rosa, L. R. V. e Silva, G. B. Longato, A. F. Evangelista, I. N. F. Gomes, A. L. V. Alves, B. G. de Oliveira, F. E. Pinto, W. Romão, A. R. de Rezende, A. A. C. Araújo, L. S. F. M. Oliveira, A. A. d. M. Souza, S. C. Oliveira, R. I. M. d. A. Ribeiro, V. A. O. Silva, R. M. Reis, *Int. J. Mol. Sci.* **2021**, *22*, 3383.
[15] M. Valli, H. M. Russo, V. S. Bolzani, *An. Acad. Bras. Cienc.* **2018**, *90*, 763–778.
[16] A. Korda, L. Rárová, Z. Pakulski, M. Strnad, J. Oklešťková, K. Kuczynska, P. Cmoch, K. Gwardiak, R. Karczewski, *Bioorg. Chem.* **2020**, *100*, 103868.
[17] M. Madej, J. Gola, E. Chrobak, *Pharmaceutics* **2023**, *15*, 2768.
[18] A. Ostapiuk, Ł. Kurach, M. Strzemski, J. Kurzepa, A. Hordyjewska, *Molecules* **2021**, *26*, 4633.
[19] S. Amiri, S. Dastghaib, M. Ahmadi, P. Mehrbod, F. Khadem, H. Behrouj, M.-R. Aghanoori, F. Machaj, M. Ghamsari, J. Rosik, A. Hudecki, A. Afkhami, M. Hashemi, M. J. Los, P. Mokarram, T. Madrakian, S. Ghavami, *Biotechnol. Adv.* **2020**, *38*, 107409.
[20] E. Chrobak, E. Bębenek, M. Kadela-Tomanek, M. Latocha, C. Jelsch, E. Wenger, S. Boryczka, *Molecules* **2016**, *21*, 1123.
[21] A. Ç. Karagöz, M. Leidenberger, F. Hahn, F. Hampel, O. Friedrich, M. Marschall, B. Kappes, S. B. Tsogoeva, *Bioorg. Med. Chem.* **2019**, *27*, 110–115.
[22] L. Pohjala, S. Alakurtti, T. Ahola, J. Yli-Kauhaluoma, P. Tammela, *J. Nat. Prod.* **2009**, *72*, 1917–1926.
[23] S. Alakurtti, T. Mäkelä, S. Koskimies, J. Yli-Kauhaluoma, *Eur. J. Pharm. Sci.* **2006**, *29*, 1–13.
[24] M. Grymel, A. Lalik, A. Kazek-Kęsik, M. Szewczyk, P. Grabiec, K. Erfurt, *Molecules* **2022**, *27*, 5156.
[25] F. O. Adepoju, K. C. Duru, E. Li, E. G. Kovaleva, M. V. Tsurkan, *Biomolecules* **2023**, *13*, 1105.
[26] H. O. B. Oloyede, H. O. Ajiboye, M. O. Salawu, T. O. Ajiboye, *Microb. Pathog.* **2017**, *111*, 338–344.
[27] P. Šiman, A. Filipová, A. Tichá, M. Niang, A. Bezrouk, R. Havelek, *PLoS One* **2016**, *11*, e0154933.
[28] S.-Y. Zhang, Q.-F. Zhao, N.-N. Fang, J.-G. Yu, *Eur. Rev. Med. Pharmacol. Sci.* **2015**, *19*, 455–60.
[29] X. Ci, J. Zhou, H. Lv, Q. Yu, L. Peng, S. Hua, *Cell Death Dis.* **2017**, *8*, e2798–e2798.


© 2025 The Author(s). ChemistrySelect published by Wiley-VCH GmbH

[30] S. Boryczka, E. Bębenek, J. Wietrzyk, K. Kempińska, M. Jastrzębska, J. Kusz, M. Nowak, *Molecules* **2013**, *18*, 4526–4543.
[31] S. K. Król, M. Kiełbus, A. Rivero-Müller, A. Stepulak, *Biomed Res. Int.* **2015**, *2015*, 1–11.
[32] M. Grymel, M. Zawojak, J. Adamek, *J. Nat. Prod.* **2019**, *82*, 1719–1730.
[33] D. Cao, G. Zhao, W. Yan, *J. Chem. Eng. Data* **2007**, *52*, 1366–1368.
[34] T. N. Drebushchak, M. A. Mikhailenko, M. E. Brezgunova, T. P. Shakhtshneider, S. A. Kuznetsova, *J. Struct. Chem.* **2010**, *51*, 798–801.
[35] M. Kadela-Tomanek, M. Jastrzębska, K. Marciniec, E. Chrobak, E. Bębenek, S. Boryczka, *Pharmaceutics* **2021**, *13*, 781.
[36] Z. Rzepka, K. Bober-Majnusz, J. M. Hermanowicz, E. Bębenek, E. Chrobak, A. Surażyński, D. Wrześniok, *Molecules* **2024**, *29*, 4408.
[37] E. Bębenek, Z. Rzepka, J. M. Hermanowicz, E. Chrobak, A. Surażyński, A. Beberok, D. Wrześniok, *Int. J. Mol. Sci.* **2024**, *25*, 4517.
[38] Bruker, Bruker AXS LLC preprint, **2016**.
[39] L. Krause, R. Herbst-Irmer, G. M. Sheldrick, D. Stalke, *J. Appl. Crystallogr.* **2015**, *48*, 3–10.
[40] G. M. Sheldrick, *Acta Crystallog.r A Found Adv.* **2015**, *71*, 3–8.
[41] G. M. Sheldrick, *Acta Crystallogr. C Struct. Chem.* **2015**, *71*, 3–8.
[42] O. V. Dolomanov, L. J. Bourhis, R. J. Gildea, J. A. K. Howard, H. Puschmann, *J. Appl. Crystallogr.* **2009**, *42*, 339–341.
[43] C. F. Macrae, I. Sovago, S. J. Cottrell, P. T. A. Galek, P. McCabe, E. Pidcock, M. Platings, G. P. Shields, J. S. Stevens, M. Towler, P. A. Wood, *J. Appl. Crystallogr.* **2020**, *53*, 226–235.
[44] A. L. Spek, *J. Appl. Crystallogr.* **2003**, *36*, 7–13.
[45] C. R. Groom, I. J. Bruno, M. P. Lightfoot, S. C. Ward, *Acta Crystallogr. B Struct. Sci. Cryst. Eng. Mater.* **2016**, *72*, 171–179.
[46] T. Langer, G. Wolber, *Drug Discov. Today Technol.* **2004**, *1*, 203–207.
[47] T. Lu, Q. Chen, in *Conceptual Density Functional Theory*, Wiley, Durham, NC **2022**, pp. 631–647, https://doi.org/10.1002/9783527829941.
[48] *The Quantum Theory of Atoms in Molecules* (Eds: C. F. Matta, R. J. Boyd), Wiley, Weinheim, German **2007**, https://doi.org/10.1002/9783527610709.
[49] D. A. Filimonov, A. A. Lagunin, T. A. Gloriozova, A. V. Rudik, D. S. Druzhilovskii, P. V. Pogodin, V. V. Poroikov, *Chem. Heterocycl. Compd. (N Y)* **2014**, *50*, 444–457.
[50] A. Daina, O. Michielin, V. Zoete, *Sci. Rep.* **2017**, *7*, 42717.
[51] G. Wolber, T. Langer, *J. Chem. Inf. Model.* **2005**, *45*, 160–169.
[52] J. Bernstein, R. E. Davis, L. Shimoni, N.-L. Chang, *Angew. Chem. Int. Ed. Eng.* **1995**, *34*, 1555–1573.
[53] N. M. DeVore, E. E. Scott, *Nature* **2012**, *482*, 116–119.
[54] G. Snaterse, A. E. Taylor, J. M. Moll, D. M. O'Neil, W. J. Teubel, W. M. van Weerden, W. Arlt, J. Hofland, *J. Steroid Biochem. Mol. Biol.* **2024**, *236*, 106446.
[55] P. Perumal, S. Dhanasundaram, A. Aravinth, C. Kamaraj, P. Santhanam, R. Rajaram, *South Afr. J. Bot.* **2023**, *163*, 443–456.
[56] C. M. Şoica, C. A. Dehelean, C. Peev, M. Aluas, I. Zupkó, P. Kása, E. Alexa, *Nat. Prod. Res.* **2012**, *26*, 968–974.
[57] E. Chrobak, M. Kadela-Tomanek, E. Bębenek, K. Marciniec, J. Wietrzyk, J. Trynda, B. Pawełczak, J. Kusz, J. Kasperczyk, E. Chodurek, P. Paduszyński, S. Boryczka, *Bioorg. Chem.* **2019**, *87*, 613–628.
[58] A. S. N. de Aguiar, L. B. R. de Carvalho, C. M. Gomes, M. M. Castro, F. S. Martins, L. L. Borges, *Pharmaceuticals* **2025**, *18*, 410.
[59] O. Artigalás, T. Vanni, M. H. Hutz, P. Ashton-Prolla, I. V. Schwartz, *BMC Med.* **2015**, *13*, 139.
[60] A. Li-Wan-Po, T. Girard, P. Farndon, C. Cooley, J. Lithgow, *Br. J. Clin. Pharmacol.* **2010**, *69*, 222–230.

Manuscript received: June 3, 2025


© 2025 The Author(s). ChemistrySelect published by Wiley-VCH GmbH